J. Fluid Mech. (1975), *vol.* 69, *part* 1, *pp.* 41–64
Printed in Great Britain

The 'sliced-cylinder' laboratory model of the wind-driven ocean circulation.
Part 2. Oscillatory forcing and Rossby wave resonance

By ROBERT C. BEARDSLEY

Department of Meteorology, Massachusetts Institute of Technology, Cambridge

(Received 7 March 1974)

The response of the 'sliced-cylinder' laboratory model for the wind-driven ocean circulation is studied here in part 2 for the case of an oscillatory 'wind' stress. The model consists of a rapidly rotating right cylinder with a planar sloping bottom. This basin geometry contains no closed geostrophic contours, so that low frequency topographic Rossby wave modes possessing mean vorticity exist in the sliced-cylinder model by the physical analogy between topographic vortex stretching and the β effect for large-scale planetary flows. The interior flow in the laboratory model is driven by the time-dependent Ekman-layer suction produced by the periodic relative angular velocity of the upper lid. The frequency of the forcing is sufficiently small that the interior motion is quasi-geostrophic with the horizontal velocities being independent of depth. Simple two-dimensional analytic and numerical models are developed and compared very favourably with the laboratory results. The observed horizontal velocity field exhibits both (i) westward intensification and decreased horizontal scale when the forcing frequency is decreased, and (ii) a significant resonant magnification when the forcing frequency is tuned to the natural frequency of one of the lower inviscid topographic Rossby wave modes. The observed westward phase speed of the driven motion is accurately predicted and shows little dependence on the amplitude of the forcing. The instantaneous and mean Lagrangian fluid particle trajectories were measured in the laboratory model. The general derivation by Moore (1970) of the governing equations for the mean Lagrangian motion are extended to incorporate forcing and Ekman-layer dissipation. The results suggest that the mean Lagrangian flow should be significantly reduced near resonant frequencies, since the mean Eulerian motion is partially offset by the Stokes drift associated with the topographic Rossby wave modes. This result is consistent with the small observed amplitude of the mean Lagrangian motion. Also presented are the results for a laboratory experiment conducted using a combined steady and oscillatory 'wind' stress.

1. Introduction

We focus our attention in part 2 on the 'sliced-cylinder' laboratory model for the wind-driven ocean circulation and the time-dependent flows driven in it by oscillatory 'wind' stresses. The model consists of a rapidly rotating cylinder with

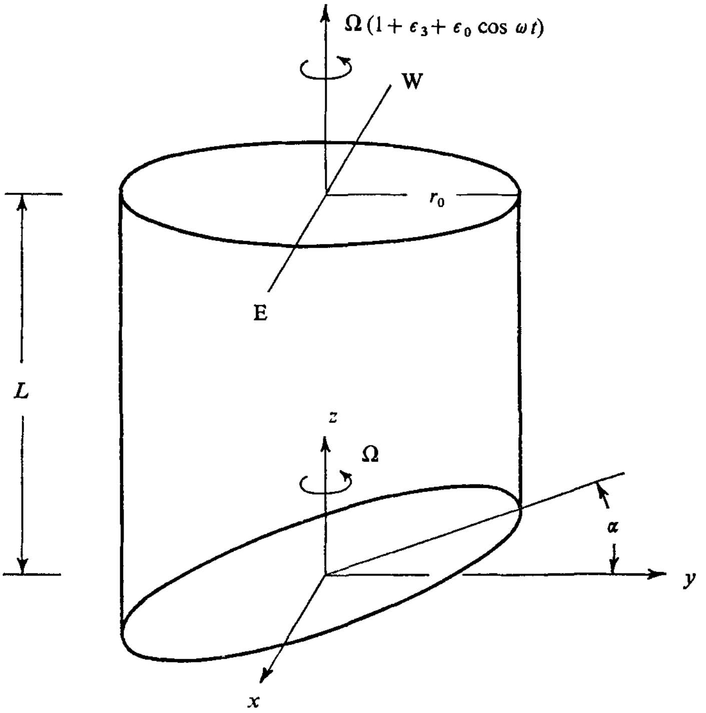

FIGURE 1. The 'sliced-cylinder' configuration.

a planar sloping bottom (see figure 1 and Beardsley & Robbins 1975 (part 1)). It was introduced by Pedlosky & Greenspan (1967), to demonstrate how the general theory for contained homogeneous rotating flows developed by Greenspan (as summarized in Greenspan 1968) must be modified for a fluid basin with no closed curves of constant depth (i.e. a basin with no closed geostrophic contours). Steady geostrophic motion can no longer exist, and is replaced by a set of new low-frequency inertial modes with frequency proportional to the bottom slope s. These modes or standing waves possess mean vorticity. They collapse into the steady geostrophic mode in the limit of zero bottom slope $s = 0$. Owing to the physical analogy between topographic vortex stretching in the 'sliced-cylinder' model and the β effect for large-scale geophysical flows, these inertial waves are dynamically similar to atmospheric planetary waves first studied by Rossby (1939). In the context of the sliced-cylinder and similar models, they will be called *topographic Rossby* waves. Pedlosky & Greenspan (1967) used these quasi-geostrophic modes to solve the initial-value problem for spin-up in the sliced-cylinder geometry. (See Greenspan (1968, p. 91) for a visual comparison of theory and experiment for spin-up.) Since the 'sliced-cylinder' geometry possesses these low-frequency modes, our approach has been to use this particular laboratory model to examine the forced response of weakly-damped topographic Rossby waves.

Other laboratory geometries besides the sliced-cylinder model can be used to simulate Rossby waves. Both Ibbetson & Phillips (1967) and Holton (1971) have used an annular basin with a prescribed radial depth variation to study forced barotropic Rossby waves. The first study is based on an analysis by Phillips (1965) of the free topographic travelling waves in a rotating annulus with a free surface such that the depth is proportional to radius squared. This particular choice of geometry leads to simple analytic solutions, which are then compared with experiments by Ibbetson & Phillips (1967). In the 'open' channel experiment, a flat paddle placed vertically in the annulus was used to excite waves propagating in both directions along the channel. The experiments nicely verified that long waves (with positive group velocity) were generated on the up-rotation side of the paddle, while shorter waves (with negative group velocity) appeared on the down-rotation side. Both sets of wave trains possessed westward phase velocities (in the down-rotation direction). The viscous damping was sufficiently large that the two wave trains were dissipated before meeting on the opposite side of the annulus; hence the phase 'open' channel. The observed rate of damping was larger (by 20 to 100 %) than predicted by an analysis of the Ekman and side-wall boundary layers. This large damping also prohibited any pronounced resonance in the 'closed' channel experiment conducted with a radial barrier located 60° up-rotation of the paddle. These experiments did illustrate the frequency-dependent east–west asymmetry in the forced Rossby wave response, as predicted in a separate study of forced β-plane modes by Pedlosky (1965). A significant mean azimuthal circulation was also observed (see Ibbetson & Phillips 1967, figure 5 (*b*)), in part because of a large Stokes drift associated with the large paddle amplitudes used in the experiment.

More recently, Holton (1971) considered topographic waves in a rotating annulus with a linear sloping bottom. The waves were forced by a simple mass source–sink distribution which was rotated in a westward sense relative to the annulus. The experiments illustrated in a qualitative way that different free modes are resonantly excited as their westward phase speeds are matched by the relative rotation of the source–sink distribution. The actual concentrated nature of the source–sink distribution (and the strong nonlinear flows near it) prohibited any detailed comparison of the experimental results with Holton's linear analysis.

These previous laboratory studies have served to demonstrate some of the major features of forced quasi-geostrophic motion in connexion with the barotropic wind-driven ocean circulation problem. Quasi-geostrophic motion in the ocean has, of course, been the subject of much study in the past fifteen years. The particular question of the influence of low-frequency fluctuating motions on the mean general circulation has become a central question on which, hopefully, MODE (Mid-Ocean Dynamics Experiment) and similar experiments will provide some insight. Much of this interest has been stimulated by the early observations of Swallow (1961) and Crease (1962), indicating that there is significantly more meridional eddy motion in the western part of the Atlantic Ocean than in the eastern. Phillips (1966) later fitted some of the Swallow float observations taken near Bermuda to a two-layer model. This necessarily crude analysis indicated that almost 80 % of the kinetic energy is in the barotropic mode. More recent observations indicate that most of the kinetic energy contained in the low-frequency band is in the barotropic and first baroclinic modes. The theoretical study of ocean circulations in closed basins driven by oscillatory wind stresses began with Pedlosky (1965), who determined the linear response in a barotropic β-plane model to an easterly moving stress pattern. Phillips (1966) extended this linear analysis to a two-layer model and examined in detail the very low-frequency response, in an attempt to explain the Swallow float observations as overdamped Rossby modes. Another aspect of the theoretical problem has been examined by Robinson (1965), Pedlosky (1965), and Munk & Moore (1968), who computed in a variety of inviscid models steady mean circulations driven by Reynolds stresses produced by low-frequency fluctuations. Veronis, in a sequence of more sophisticated numerical models (summarized in 1970), has also studied the generation of mean currents driven by large amplitude oscillatory wind stresses. The mean circulations examined in these previous studies have all been time average currents in the Eulerian sense (i.e. time average currents observed at a fixed position in space). Moore (1970) examined both the mean circulation driven by the Reynolds stresses plus the Stokes drift associated with the inviscid wave motion, to deduce that the mean Lagrangian velocity must satisfy both the linearized potential vorticity and continuity equations for unforced steady flow. This result applied to containers with *open* geostrophic contours means that the Stokes drift for each of the free modes will exactly cancel the associated mean Eulerian circulation, to produce a *zero* mean Lagrangian motion. Unfortunately, Moore's analysis cannot easily be extended to the case of forced motion in a dissipative system. But, in the case discussed by Pedlosky (1965), where the forced motion at resonance has the structure of an inviscid free mode, Moore argues that the Lagrangian mean velocity should vanish to second order. This result is not true when the rate of damping is large enough to modify the modal structure near resonance.

We shall now consider the low-frequency transient motion generated in the sliced-cylinder model by an oscillatory forcing. In the laboratory model (see figure 1), the *relative* angular velocity of the driving lid is represented by

$$\Omega_{\mathrm{rel}}/\Omega = \epsilon_s + \epsilon_0 \cos \omega t. \tag{1}$$

Ω is the angular velocity of the basin; ϵ_s and ϵ_0 are the non-dimensional Rossby numbers associated with the steady and periodic components of the external forcing. Our principal interest is in a purely sinusoidal forcing with $\epsilon_s = 0$, although the results of exploratory experiments with both steady and oscillatory forcing will be presented. In § 2 a simple analytic model will be developed from the model equations presented in part 1. The analytic solutions will then be compared with results from both laboratory and numerical experiments. Then some observations of the mean Lagrangian velocity will be discussed.

2. The analytic model

We wish to develop a simple analytic model for the time-dependent motion, forced mechanically in the sliced-cylinder geometry by a relative angular oscillatory motion of the upper lid. A consistent two-dimensional vorticity equation for low-frequency motion in the sliced-cylinder model was derived in part 1. We shall use here a modified version of (8), in which (i) velocity and time are scaled by $\epsilon_0 \Omega L$ and Ω^{-1}, respectively, and (ii) the effects of lateral friction are ignored. This scaling is chosen to be consistent with Pedlosky & Greenspan's analysis of the free topographic Rossby modes in the sliced-cylinder model. Justification for both the continued use of steady Ekman-layer theory to couple the motion in the interior of the fluid to the mechanical forcing and the neglect of lateral vorticity diffusion will be presented later. The resulting linearized governing vorticity equation in this new scaling is then

$$(\partial/\partial t + \gamma)\nabla^2\psi_0 + S\psi_{0x} = \gamma \cos \sigma t. \tag{2}$$

The non-dimensional decay rate due to Ekman-layer suction is $\gamma = 2E^{\frac{1}{2}}$ ($E = \nu/\Omega L^2$); the non-dimensional coefficient for the topographic β effect is $S = 2s$ (where $s = \tan\alpha$ is the bottom slope); and σ is simply the ratio of the forcing frequency ω divided by Ω. The only boundary condition on ψ_0 is that the cylindrical boundary at $r = a$ be a streamline, thus $\psi_0 = 0$ there. Equation (2) is similar to the linearized β-plane vorticity equations studied by Pedlosky (1965) and Phillips (1966), the sole difference occurring in the spatial structure of the forcing.

In the inviscid limit with $\gamma \rightarrow 0$, (2) reduces to the linearized conservation equation for potential vorticity with free topographic Rossby modes as solutions. The form of these normal modes is given by

$$\psi_{0_{mn}} = J_m(k_{mn} r/a) \exp i(m\theta + k_{mn} x/a + \sigma_{mn} t), \tag{3}$$

and the dispersion relationship is

$$\sigma_{mn} = sa/k_{mn}, \tag{4}$$

where $J_m(k_{mn}) = 0$. These modes consist of westward propagating vorticity cells with a stationary amplitude envelope given by the individual Bessel functions. As the spatial scale decreases with increasing n and m, the effective topographic restoring force decreases, causing the natural frequency of the modes to decrease. By analogy to simple mechanical systems (see Slater & Frank 1947), we can use the natural period of the free modes together with the Ekman-layer spin-down rate to define a quality factor for the damped modes

$$Q_{nm} = \frac{\sigma_{nm}}{2\gamma} = \frac{sa}{4E^{\frac{1}{2}} k_{nm}}.$$

Q is 2π times the reciprocal fractional loss of energy over one wave period. When $Q \gg 1$, a sharp resonance occurs in the slightly dissipative system when driven at the natural frequency. For the range of parameters explored here, the maximum $Q = 10$ for the lowest topographic Rossby mode ($m = 0$, $n = 1$). Q tends to zero for the higher modes, owing to the increase in period with decreasing spatial scale.

The analytic solution to the forced viscous vorticity equation (2) may be obtained in terms of elementary functions as

$$\psi_0 = -\operatorname{Re}\left[\frac{\gamma a}{S}\exp(i\sigma t)\left(\frac{x}{a} + i\frac{J_1(\lambda)}{J_0(\lambda)}\exp(ikx)\, J_0(kr) - \sum_{m=1}^{\infty} C_m J_m(kr) \cos m\theta \exp(ikx)\right)\right], \tag{5}$$

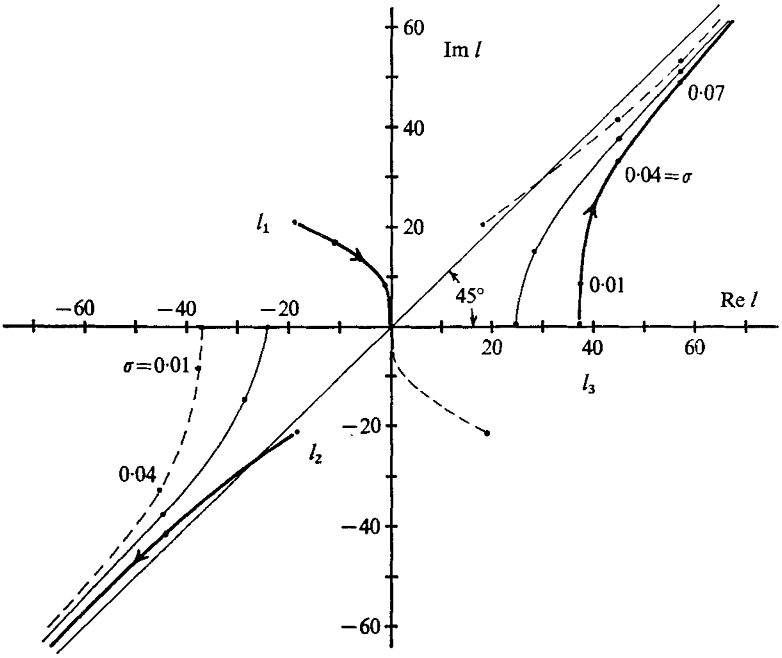

FIGURE 2. Roots of boundary-layer equation (6) plotted for azimuthal positions $\theta = 0$ (------), $\frac{1}{2}\pi$ (——), π (———), as a function of relative forcing frequency ω/Ω.

where the Fourier coefficients and the complex wavenumber are defined by

$$C_m = (-i)^{m+1}\frac{(J_{m-1}(\lambda)-J_{m+1}(\lambda))}{J_m(\lambda)},$$

$$k = \tfrac{1}{2}Si(\gamma+i\sigma), \quad \lambda = ka.$$

The full solution consists of a particular forced north–south motion plus the superposition of damped modes (similar but not identical in structure to the free modes) required here by the boundary condition on the forced flow. The east–west wavenumber k is complex. We used the MIT Information Processing Center subroutine Combes to compute numerical values of the J Bessel function for complex arguments.

The above solution is based on two assumptions: the applicability of the steady-state Ekman-suction formula, and the neglect of lateral friction. Since our interest lies in the low-frequency motion for which $\sigma = \omega/\Omega \ll 1$, the time-dependent Ekman-layer problem may be solved using a perturbation approach (with σ being the small parameter), to yield a first-order Ekman-layer suction formula for low-frequency motion. The slow but non-steady time dependence of the motion causes a small amplitude and phase difference in the Ekman-layer suction. For the range of parameters and frequencies considered here, the amplitude difference is insignificant, while the computed phase lag between the interior vorticity field and the Ekman-layer suction never exceeds 3°. Thus the simplicity of using the steady-state Ekman-layer suction formula in developing (2) is really justified as a sufficiently accurate approximation for our model problem.

The fluid must also satisfy the no-slip boundary condition on the lateral boundary. For the case of a *steady* driving stress, western intensification occurs and a topographically modified $E^{\frac{1}{4}}$ Stewartson layer arises to bring the western boundary current to zero at the lateral boundary. Stokes-like boundary layers can now occur in the time-dependent case, where the boundary-layer thickness is a strong function of the forcing frequency. Let $\tilde{v} = \mathrm{Re}\sum_j v_j \exp(l_j\rho + i\sigma t)$ be the boundary-layer correction field for the azimuthal velocity, which is to be added to (5) so that the combined velocity field satisfies the no-slip condition at $r = a$. The boundary-layer co-ordinate is $\rho = a-r$. Substitution of $\tilde{v}$ into (2) yields the following eigenvalue equation for l, the inverse boundary-layer thickness scale:

$$-(i\sigma+\gamma)\,l + S\cos\theta + El^3 = 0. \tag{6}$$

$E = \nu/\Omega L^2$ is the original Ekman number. The three roots of (6) are plotted in figure 2 for three different azimuthal positions $\theta = 0, \frac{1}{2}\pi, \pi$. Near $\theta = \frac{1}{2}\pi$, the topographic influence is negligible, and the boundary-layer structure is similar to the classic Stokes layer (see Lamb 1945, § 345), with an approximate non-dimensional thickness $(E/\sigma)^{\frac{1}{2}}$. Along the eastern and western boundaries, topographic vortex stretching is important only at *very low* frequencies. For example, at $\theta = \pi$, the two allowable roots with negative real parts are l_1 and l_2 (see figure 2). In the steady limit, with $\sigma = 0$, l_1 and l_2 are complex conjugates representing the topographically modified $E^{\frac{1}{4}}$ Stewartson layer. As the frequency increases, l_1 decreases rapidly towards zero, while l_2 increases rapidly and approaches the $-\frac{3}{4}\pi$ asymptote characterizing the classic Stokes boundary layer. The amplitude of the correction field $\tilde{v}_1$ associated with l_1 also decreases rapidly toward zero, while $-\tilde{v}_2$ rapidly approaches the interior tangential velocity value with increasing frequency. Only one root of (6) has a negative real part along the eastern boundary. The structure there again approaches the classic Stokes behaviour for increasing frequency. For the range of frequencies studied here, these time-dependent lateral boundary layers are still relatively thin (e.g. $\Delta\rho = -1/\mathrm{Re}\,(l_2) = \frac{1}{40}$ at $\sigma = 0{\cdot}04$, or approximately 0·25 cm). In the (relatively) high-frequency limit, both the ratios of the boundary-layer scale thickness and inverse velocity amplitudes are proportional to $l_1 l_2^{-1} \simeq E^{\frac{1}{2}}\sigma^{-\frac{3}{2}} \simeq 0{\cdot}12$ for $\sigma = 0{\cdot}07$. Scale analysis suggests that lateral friction is completely negligible in the interior, owing to the large spatial scales associated with the lower topographic Rossby modes.

3. The experiments

We next discuss the laboratory and numerical sliced-cylinder experiments for transient forcing and compare the experimental results with the preceding analytic solution. The basic sliced-cylinder laboratory apparatus has been described in detail in Beardsley (1969). The fluid motion is driven by the oscillatory relative rotation of the upper lid, which is generated through a gear train, by a simple synchronous motor and scotch-yoke mechanism. In most of the experiments to be presented, we chose for the sake of simplicity to hold *constant*

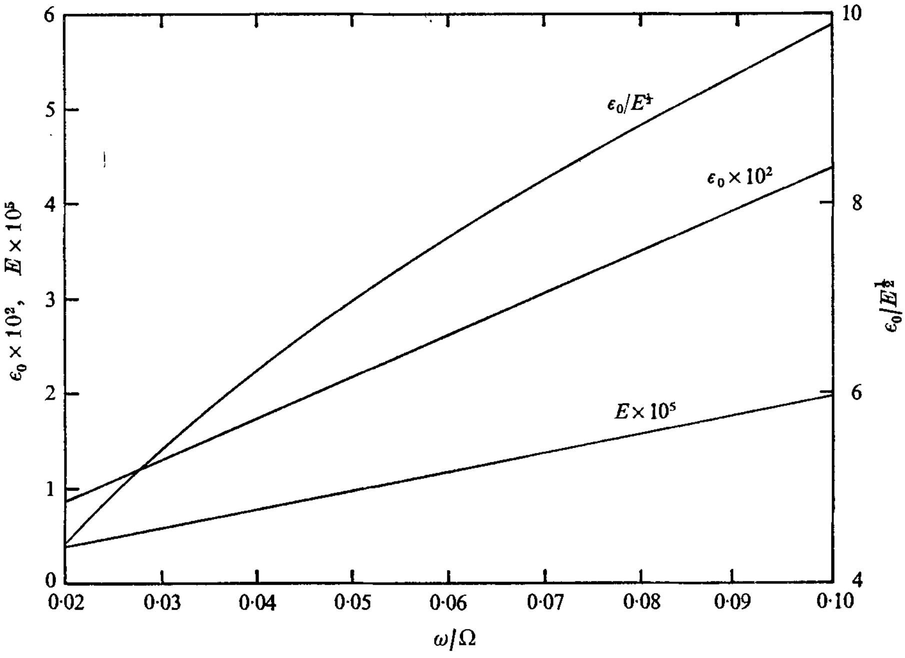

FIGURE 3. External parameter variation as a function of relative forcing frequency $\sigma \equiv \omega/\Omega$. Rossby number $\epsilon_0 = 0{\cdot}0304$ at $\omega/\Omega = 0{\cdot}07$.

both the absolute frequency of the forcing and the relative angular velocity of the driving lid. Thus the rotation of the synchronous motor is kept at 3 r.p.m., so that the absolute forcing frequency is $\omega = 0{\cdot}314\,\mathrm{rad\,s^{-1}}$. In many of the experiments, the amplitude of the relative angular velocity is fixed at $\epsilon_0 \Omega = 0{\cdot}137\,\mathrm{rad\,s^{-1}}$, corresponding to a total angular displacement of the lid of 2·74 rad (or 156°) in half a period. With this mechanical arrangement, both the relative forcing frequency $\sigma = \omega/\Omega$, and the external oscillatory Rossby number ϵ_0 are varied inversely by adjusting the overall angular velocity of the basin, Ω. The dependence of the various external experimental parameters on the relative forcing frequency are illustrated in figure 3. A differential gear plus an independent synchronous motor in the gear train can also allow the addition of a steady component to the sinusoidal driving. This feature is used to study the influence of transient waves on the intense western boundary current.

The typical interior velocities were large enough that the horizontal flow structure was visualized with streak photography, using a weak aluminium flake suspension illuminated from the side by a narrow horizontal slit beam, centred at a depth of $z = 0{\cdot}43$. An automatic 35 mm camera was used to take a time-lapse photograph (with an exposure of 2·1 s) every 21 s. With the basic oscillatory period $(2\pi/\omega)$ fixed at 20 s, the automatic camera produced a sequence of 20 streak photographs, to illustrate the horizontal flow field over one wave period.

An attempt was made to measure horizontal velocities using heated miniature thermistors as constant-temperature hot-wire anemometers. Three thermistors (VECO 31A45, nominal resistance 1 K, diameter 0·033 cm) were suspended along the east–west axis of the cylinder at $x/L = -1/\surd 2$, 0, $1/\surd 2$ near the midplane of the basin at $z/L = 0{\cdot}43$. The thermistors had approximate time and dissipation constants in water of 100 ms and 2 mW $^{\circ}\mathrm{C}^{-1}$, respectively, so that maintenance of a 2 °C temperature rise above ambient temperature required only about 4 mW dissipation in the fluid. While the speed–voltage calibration for the individual thermistors varied too much with time for the velocity to be accurately measured, the greater sensitivity to low flow speeds made the thermistor anemometers a good null-velocity sensor. Since the basic time-dependent circulation pattern consists of vortical cells with north–south symmetry, the thermistors can be used to measure accurately the time of passage of velocity nodes which occur on the east–west axis. Since the absolute forcing frequency is constant for the different experiments, the time and phase lags associated with the finite response time of the thermistors should remain approximately constant and thus independent of the relative forcing frequency σ.

The numerical solutions to be discussed were obtained using the efficient implicit scheme presented in Beardsley (1973), and outlined in part 1. The governing vorticity equation was modified to incorporate the oscillatory forcing (again using the steady-state Ekman-layer suction formula), then integrated for several spin-up periods, until the starting transients had vanished. The radial grid net used was essentially uniform spacing in the interior with increased resolution near the outer boundary. The appropriate radial scale for the side-wall boundary layer is the Stokes thickness $d = L(E/\sigma)^{\frac{1}{2}}$. Beardsley (1973) gave the actual radial transformation used in these time-dependent calculations with $a = 0{\cdot}5$ and $d = (E/\sigma)^{\frac{1}{2}}$ (see that paper for the notation). This choice places approximately half the total grid points uniformly separated in the interior with the remaining grid points concentrated near the circular boundary. With a radial–azimuthal grid net of 31 × 128 points and 32 time steps used per oscillation period, the estimated spatial and temporal truncation errors were less than 0·5 % for the lower topographic modes. The efficiency of the implicit scheme was improved by sinusoidal extrapolation, to predict the new stream function and wall vorticity fields.

A list of numerical experiments conducted, together with the equivalent external laboratory parameters, is given in table 1. The bottom slope in all experiments was held constant at $s = 0{\cdot}178$ ($\alpha = 10^{\circ}$), and aspect ratio $a = 1{\cdot}0$. For fixed Ω and L, the laboratory Ekman number changed less than ± 2 % owing to fluid temperature variations from experiment to experiment. A nominal value of 1 cS for ν was used in the numerical experiments, causing the Ekman suction parameter γ in the numerical experiments to be approximately 4 % larger than in the associated laboratory experiments. This systematic difference overshadows the uncertainties in the computed values of the other experimental parameters.

3.1. *The stream function and velocity*

Pedlosky (1965) and Phillips (1965) have already shown that the driven Rossby wave modes in a rectangular basin exhibit an east–west asymmetry, owing to the inclusion of Ekman-layer suction or bottom friction in their models. This feature becomes more pronounced as the relative frequency of the symmetric

Exp.	$\sigma = \omega/\Omega$	ϵ_0	$E \times 10^5$	$R_0 \times 10^3$	$\delta \times 10^2$	$\hat{E} \times 10^5$
30	0·07	0·0304	1·38	1·78	2·09	3·88
31	0·07	0·0912	1·38	5·35	2·09	3·88
32	0·0625	0·0272	1·23	1·51	1·97	3·46
33	0·07	0·2737	1·38	16·05	2·09	3·88
34	0·07	0·1521	1·38	8·92	2·09	3·88
35	0·055	0·0239	1·08	1·24	1·85	3·05
36	0·0475	0·0206	0·94	0·995	1·72	2·63
37	0·04	0·0174	0·79	0·772	1·58	2·22
38	0·0775	0·0337	1·53	2·08	2·20	4·30
39	0·0850	0·0369	1·68	2·38	2·30	4·71
40	0·073	0·0317	1·44	1·90	2·13	4·05
41	0·067	0·0291	1·32	1·67	2·04	3·71
42	0·07	0·0	1·38	0·0	2·09	3·88
43	0·0325	0·0141	0·64	0·563	1·42	1·80

TABLE 1. Parameter values for numerical experiments conducted with sinusoidal forcing

forcing decreases. The analytic solution given here in (5) for the forced topographic Rossby modes in a circular basin also exhibits this east–west asymmetry. Since the model wavenumber k is complex, the real part of the exponent of $\exp(ikx)$ is simply $-(s\gamma x)/(\gamma^2+\sigma^2)$, indicating an exponential increase in the stream-function envelope towards the west, owing to the non-zero bottom friction coefficient γ. As σ, the relative forcing frequency, decreases, the east–west asymmetry clearly increases. In the limit of zero forcing frequency, the flow reduces to a steady western boundary layer of non-dimensional thickness (s/γ) and a slow interior Sverdrup-type flow, with a balance between Ekman suction and flow across the topographic contours. When the forcing frequency is non-zero but very small, the western boundary layer consists of short reflected topographic Rossby waves that are quickly damped by Ekman-layer suction before they can propagate very far to the east. As the frequency of the forced waves increases, their characteristic horizontal scale and group velocities increase, while the fractional Ekman-layer dissipation per wave period decreases. Both trends cause the east–west asymmetry to decrease; and, in the limit of very small dissipation (i.e. $Q \gg 1$) the forcing frequency may be tuned to excite a quasi-inviscid mode resonantly, which has (as indicated by (3)) a symmetric amplitude envelope in the east–west direction.

This trend towards western concentration with decreasing frequency is illustrated in the two sequences of streak photographs shown in figures 4 and 5 (plate 1). In figure 4 the lowest normal mode is excited with the forcing frequency 5·4 % below the natural frequency of the $(m = 0, n = 1)$ inviscid mode. The forcing frequency is below the eigenfrequency of the $(m = 1, n = 1)$ mode in figure 5; both the east–west spacing of the vorticity cells and the velocity amplitudes in the eastern half of the basin are reduced. In figure 6 are shown the corresponding stream-function patterns obtained using the numerical model. Both the analytic and numerical linear solutions are symmetric about the x axis, so the small tilting of the north–south streamlines near the x axis and the alternating

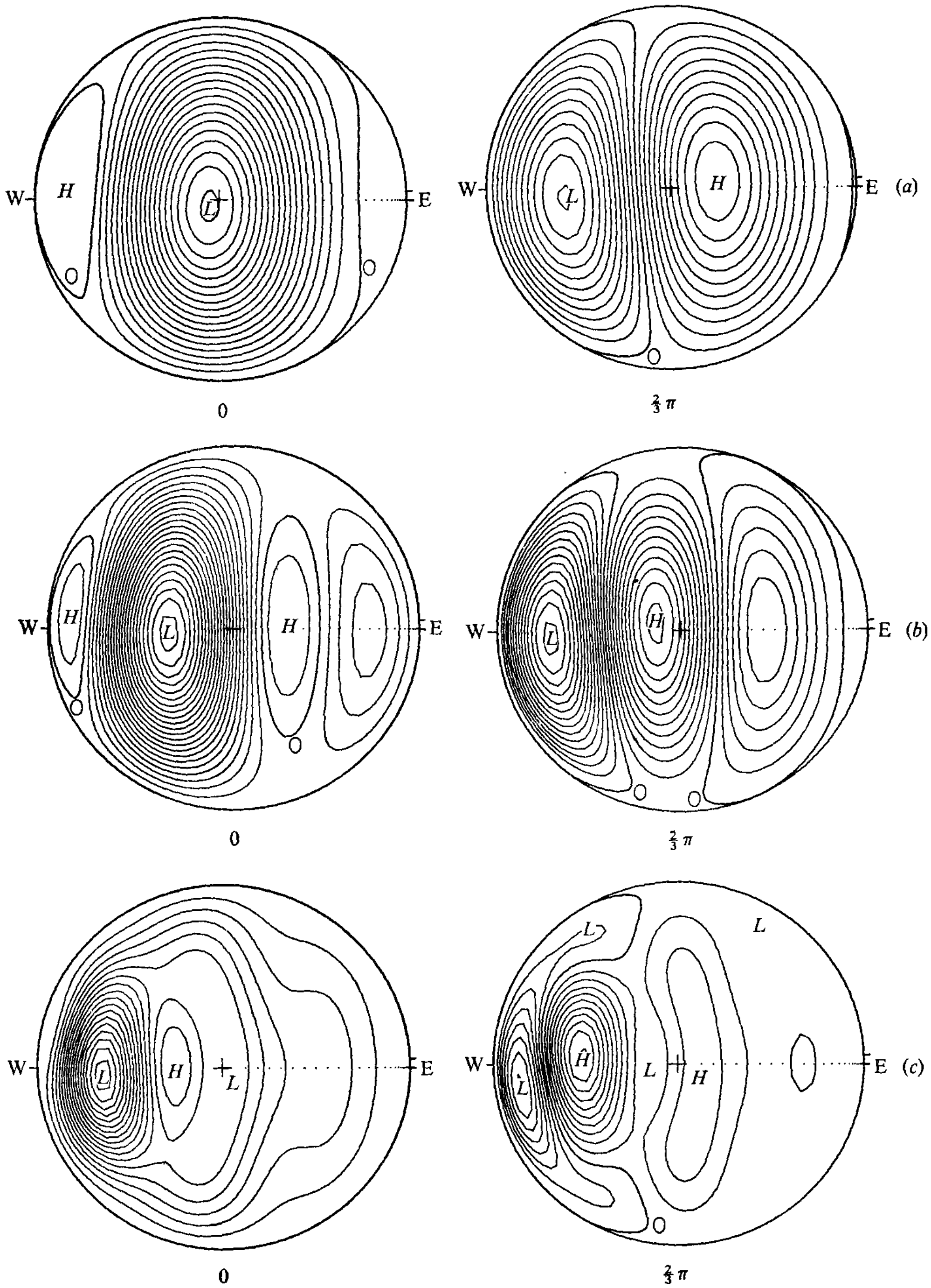

FIGURE 6. Stream-function patterns at phase lags of 0 and $\frac{2}{3}\pi$, for frequencies ω/Ω: (*a*) 0·073, (*b*) 0·055, (*c*) 0·0325. Contour interval is 20 in (*a*), (*c*), and 10 in (*b*). Extreme values are, from left to right, as follows. (*a*) $H = 40$, $L = -364$; $L = -222$, $H = 217$. (*b*) $H = 19$, $L = -223$, $H = 21$; $L = -143$, $H = 114$. (*c*) $L = -350$, $H = -63$, $L = -120$; $L = -143$, $H = 203$, $L = 5$, $H = 50$.

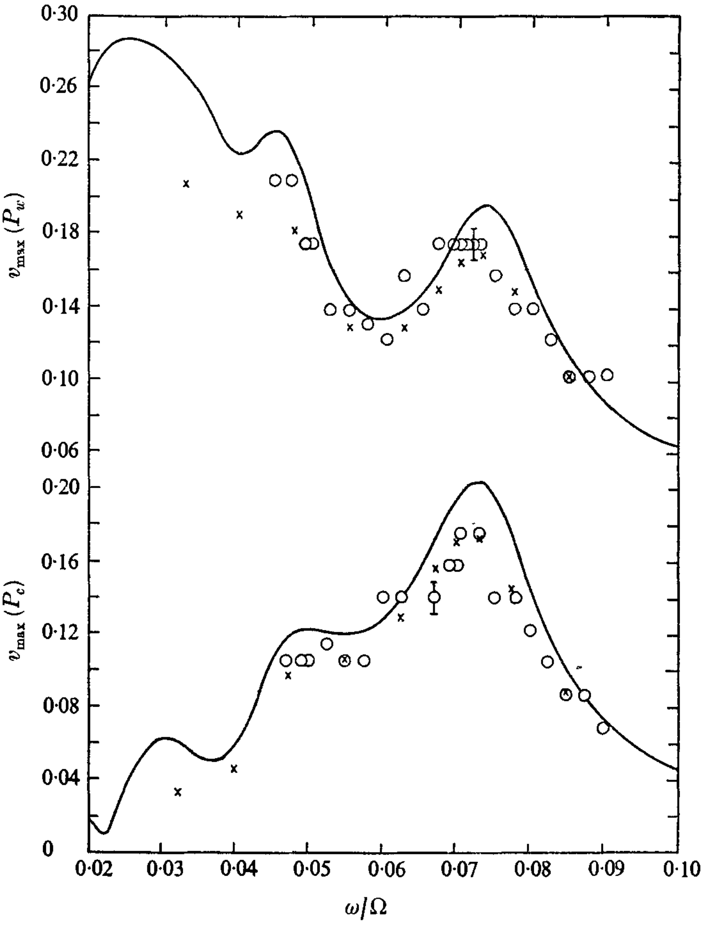

FIGURE 7. Maximum north–south velocities observed at (*a*) P_w, and (*b*) P_c, scaled by $\epsilon_0\,\Omega L$. ○, laboratory results; ×, numerical model results; ——, analytic predictions.

displacement of the highs and lows of the stream function are due to the weak nonlinearity of the flow. The second effect is more noticeable as the forcing frequency is reduced, even though in these experiments, the effective Rossby numbers (R_0 and $\epsilon_0/E^{\frac{1}{2}}$) are proportional to $\sigma^{\frac{1}{2}}$, so that the external nonlinear parameter decreases with decreasing frequency. The rapid decrease in spatial scale with decreasing frequency tends to compensate, so the nonlinear interaction of the vortical cells gets more intense at lower frequencies.

Our earlier estimation of a quality factor Q larger than unity for the lower (m, n) topographical Rossby modes in the sliced-cylinder experiment suggests that a distinct resonance may be observed when the forcing frequency is tuned to the inviscid eigenfrequencies. To demonstrate this resonance effect, we chose to measure the maximum amplitude of the north–south velocity v at two positions on the x axis: the point P_c located in the centre of the basin at $x = 0$, and the point P_w located in the western half of the basin at $x = -L/\sqrt{2}$. The observed non-dimensional velocities are shown as open circles in figure 7, together with

σ_{01}	σ_{11}	σ_{21}	σ_{02}	σ_{31}	σ_{12}
0·074	0·046	0·035	0·032	0·028	0·025

TABLE 2. Inviscid eigenfrequencies of the lower topographic Rossby wave modes in the sliced-cylinder configuration. Principal uncertainty of ± 2 % in σ_{mn} caused by error in measurement of bottom slope $s = \tan\alpha$

the analytic values (solid line) and computed values (crosses) obtained from the numerical experiments. The analytic solution clearly illustrates the peaked response near the lower eigenfrequencies $\sigma_{01} = 0{\cdot}074$ and $\sigma_{11} = 0{\cdot}046$. For the given dissipation, further decrease in the forcing frequency causes the individual modes to lose their identity, and the band structure discussed by Phillips (1966) to occur. Note that at the maximum eigenfrequency $\sigma_{01} = 0{\cdot}074$, the velocities at P_c and P_w are approximately equal, the dissipation at this frequency being sufficiently weak to cause little east–west asymmetry. The western concentration of the flow clearly occurs toward lower frequencies. The principal uncertainty in the laboratory velocity measurements arises from the difficulty of accurately determining the particle path length on the streak photographs. The streak photograph is a time-lapse picture (i.e. the particle length represents the velocity integrated over a time interval Δt equal to 10·5 % of the period of the forcing). The values of the observed velocities presented in figure 7 have been multiplied by $(\omega\Delta t)/\sin(\omega\Delta t)$, to correct for this averaging effect. In general, over the limited frequency range explored, the results of the laboratory and numerical model agree to within the estimated uncertainty while the analytic model exhibits slightly larger velocities. The linear numerical solution obtained at $\sigma = 0{\cdot}07$ indicates that, at least at this frequency, the small but non-zero inertia of the fluid reduces the maximum velocities calculated at P_c and P_w by only 0·47 %. A comparison of the maximum stream function observed at P_c and P_w is also shown in figure 8. The solid curves represent the analytic model, while the crosses are predicted by the numerical solutions. Again both models exhibit western intensification and resonance at the maximum eigenfrequencies.

3.2. *Phase and phase speed measurements*

Several exploratory laboratory experiments were conducted early in this study with an additional set of miniature thermistors mounted along the x axis just outside the lower Ekman layer. Using this set, together with the set of thermistors supported at $z/L = 0{\cdot}43$, as velocity null sensors, we measured the phase lag of the westward moving cells at the two levels. We found that, to within an estimated uncertainty of ± 4°, the horizontal velocity structure was independent of depth. We then measured the relative phase of the velocity nodes at the two points P_c and P_w (at $z/L = 0{\cdot}43$) over the frequency range $0{\cdot}02 < \sigma < 0{\cdot}1$. The results are shown as vertical crosses in figure 9, together with phase lag values (circles) estimated from the streak photographs. The solid curve and diagonal crosses represent the analytic and numerical model predictions respectively. Though there is considerable experimental uncertainty in the laboratory

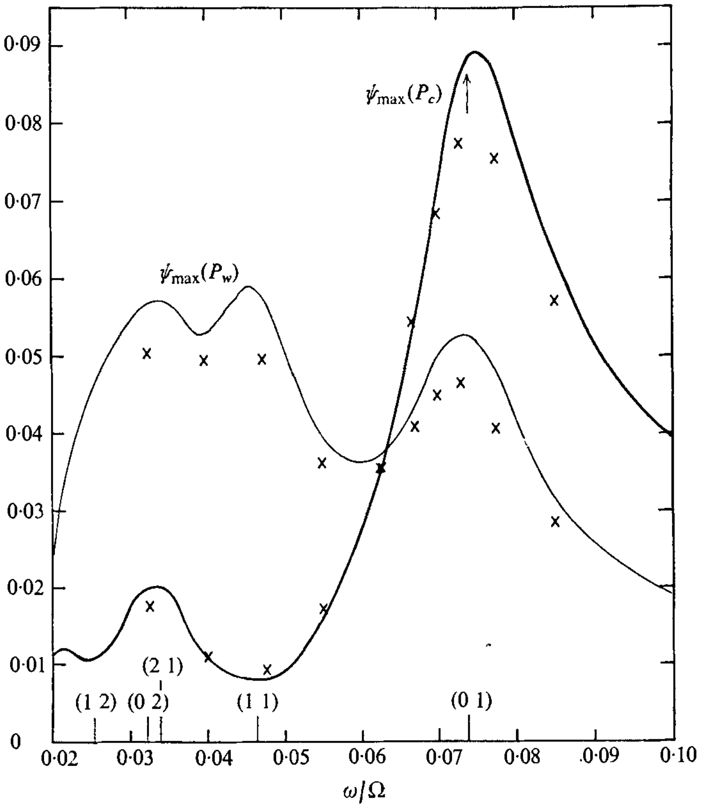

FIGURE 8. Comparison of maximum stream functions occurring at P_w and P_c as predicted by analytic model (——) and full numerical model (×).

measurements using either technique, a significant phase lag exists between the observed laboratory response and the analytic and numerical model predictions. Some lag of the same sign exhibited in figure 9 is expected, since we have assumed steady-state Ekman-layer dynamics in both theoretical models. The expected lag based on a perturbation analysis of the time-dependent Ekman layer is $< 6°$, considerably less than the observed lag. The estimated error brackets on the laboratory measurements shown in figure 9 ignore any systematic lag due to the finite time constant of the thermistors. The streak photographs are also assumed to illustrate the velocity pattern at the exact mid-time of the exposure. While the nominal phase lag for the thermistors is estimated to be less than 4°, the observed tendency for the thermistor and photographic measurements to agree more closely near resonance frequencies suggests that the thermistor measurements are highly sensitive to local flow speed.

The driven response in the sliced-cylinder model consists of vortical cells propagating westward with a phase speed which decreases monotonically with decreasing frequency. The phase lag measurements discussed previously can be used to compute the westward non-dimensional phase speed $C_p\Omega/L$ exhibited by the velocity nodes between the points P_w and P_c. The laboratory and theoretical

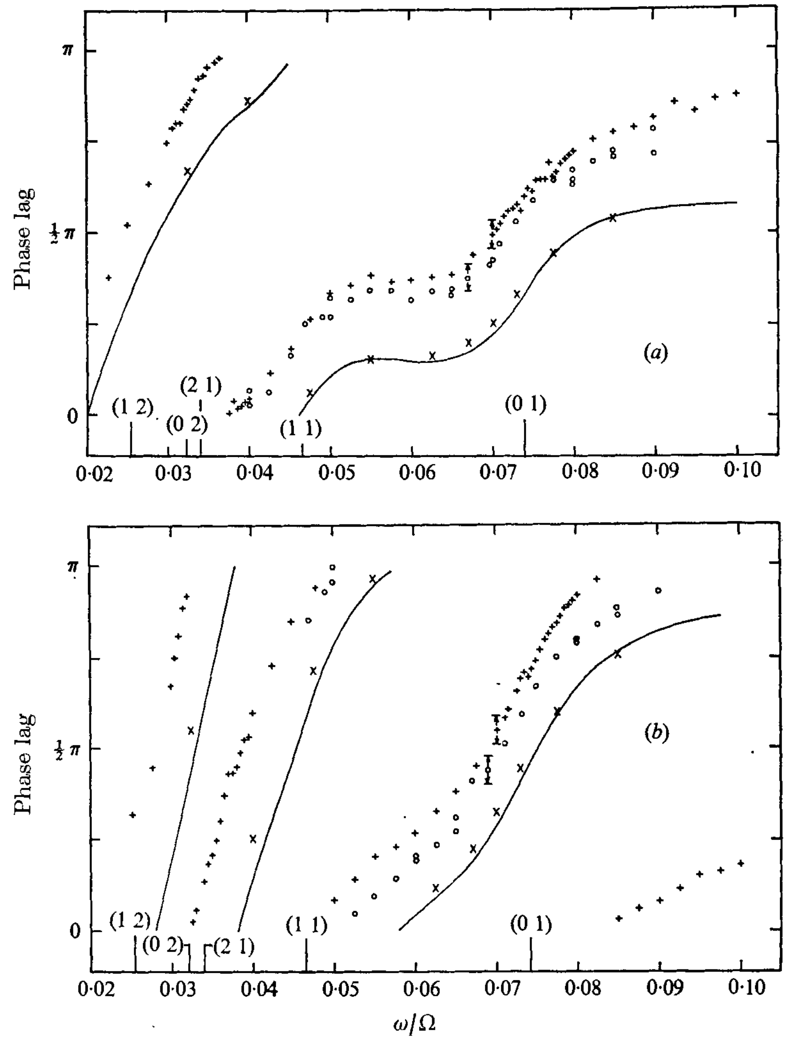

FIGURE 9. Phase lag of north–south velocity node measured at (a) P_w and (b) P_c as a function of frequency. ○, +, laboratory photographic and thermistor results; ×, numerical prediction; ——, analytic prediction.

results plotted in figure 10 show excellent agreement over most of the frequency range explored. Only at low frequencies does the percentage discrepancy increase. But, in view of the uncertainty in the thermistor technique, the low-frequency phase discrepancy between laboratory and numerical values is believed to be insignificant. (Any systematic error in the individual phase lag measurements made using the thermistor technique should cancel when the phase speed is computed using the *difference* of the observed phase lags.)

A stream-function sequence is shown in figure 11 for the case of very strong forcing near the σ_{01} eigenfrequency. With the large laboratory Rossby number $\epsilon_0 = 0{\cdot}152$, north–south asymmetry due to strong inertial effects is clearly illustrated. Increased inertia also affects the relative phase of the fluid response. The

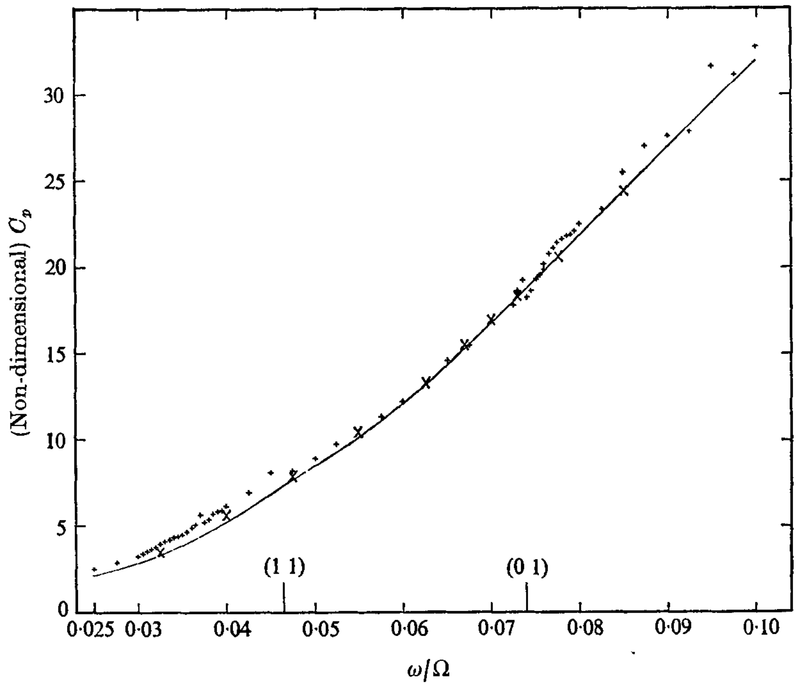

FIGURE 10. Westward phase speed scaled by ΩL against forcing frequency. +, computed from laboratory thermistor measurements; ×, numerical model prediction; ——, analytic prediction.

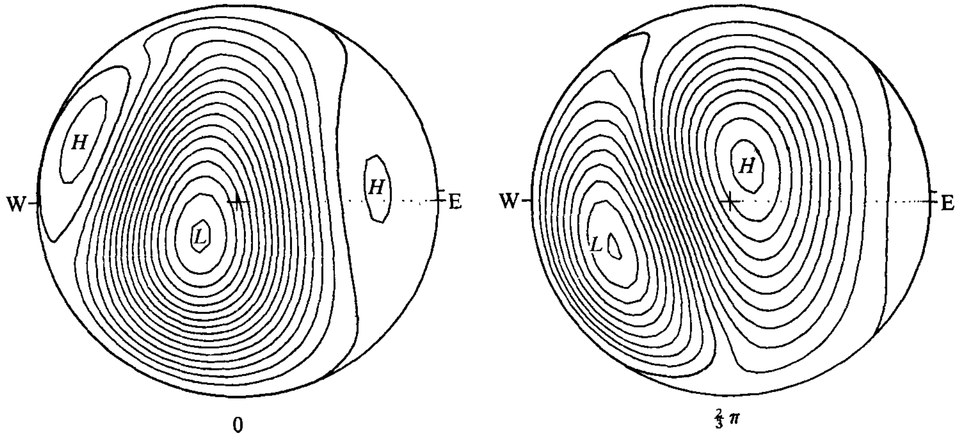

FIGURE 11. Stream-function patterns at phase lags of 0 and $\frac{2}{3}\pi$ for very strong forcing ($\epsilon_0 = 0{\cdot}152$) at $\omega/\Omega = 0{\cdot}07$. Contour interval is 20. Extreme values are, from left to right, $H = 3$, $L = -324$, $H = 22$; $L = -182$, $H = 207$.

westward phase speed, still operationally defined as the average phase speed of the north–south velocity node along the x axis between P_c and P_w, however, exhibits only a weak dependence on ϵ_0. Plotted in figure 12 against ϵ_0 are the observed phase speed values normalized by the analytic value for laboratory experiments at $\sigma = 0{\cdot}0575$, $0{\cdot}07$, and $0{\cdot}085$ and numerical experiments at $\sigma = 0{\cdot}07$. While the

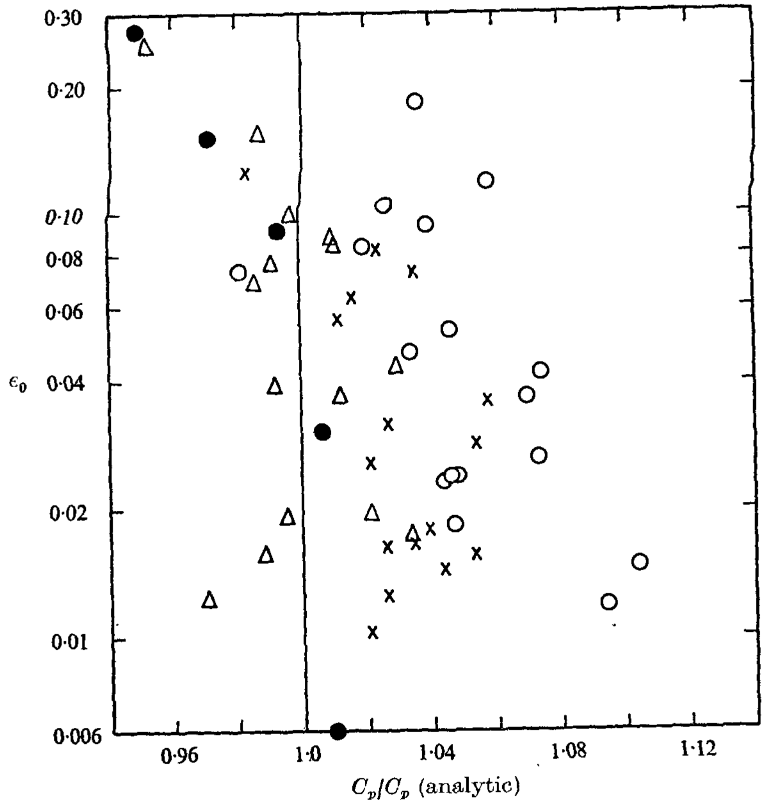

FIGURE 12. Rossby number dependence of observed phase speed normalized by predicted analytic value. ●, numerical model results. Laboratory results:

	○	△	×
ω/Ω	0·0825	0·07	0·075

numerical model exhibits a clear decreasing trend in C_p with increasing forcing, the scatter in the laboratory data prevents any significant comparison (although some of the laboratory data, especially at $\sigma = 0{\cdot}085$ and $0{\cdot}0575$, are quite suggestive). This weak dependence of C_p on ϵ_0 is a consequence of the truly inertial nature of the restoring force or β effect for Rossby waves.

3.3. *Particle motion and mean Lagrangian currents*

In the interior region of the basin, the Lagrangian particle trajectories for the sliced-cylinder modes are approximately elliptical. Several sequences of relatively short exposure streak photographs taken almost continuously were made at different forcing frequencies to determine the Lagrangian trajectories of individual aluminium flakes suspended in the fluid. A composite sketch of the observed paths for near resonant forcing at $\sigma = 0{\cdot}07$ is shown in figure 13. The laboratory Rossby number $\epsilon_0 = 0{\cdot}0304$ and the particle trajectories exhibit both a western concentration due to Ekman-layer dissipation, and a north–south asymmetry due to nonlinearity.

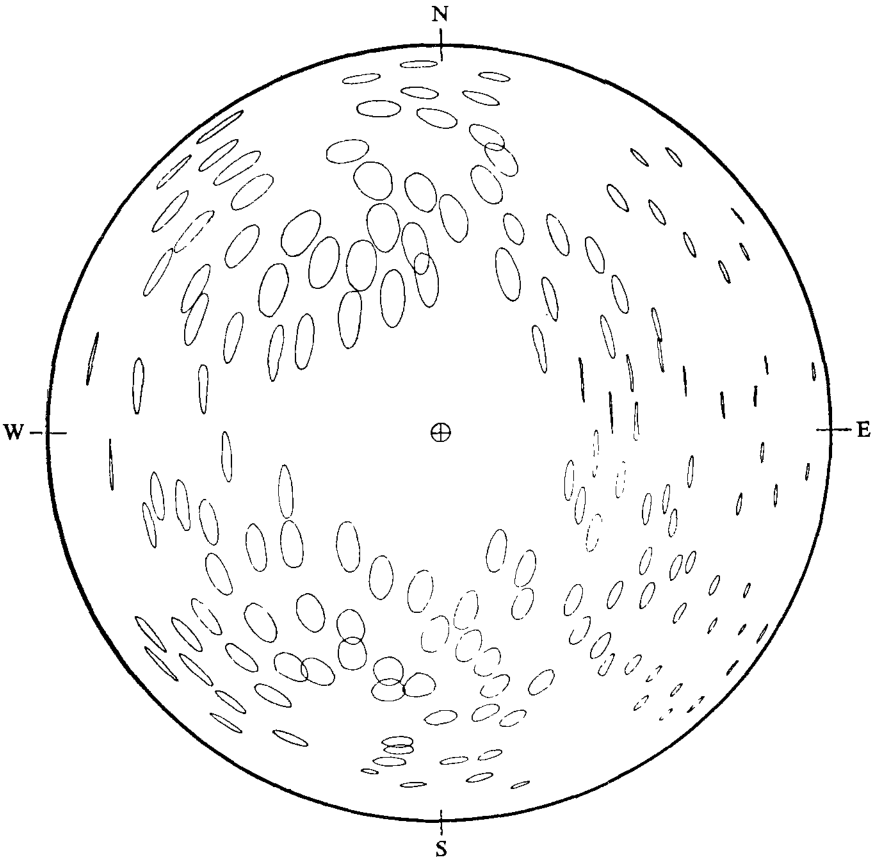

FIGURE 13. Composite sketch of Lagrangian particle path over one wave period for $\epsilon_0 = 0{\cdot}0304$, $\omega/\Omega = 0{\cdot}07$.

An attempt was also made to measure the mean Lagrangian currents by averaging the observed particle trajectories over one wave period T_w. The resulting observed mean particle displacements are plotted in figure 14(*a*) for the near resonance case of $\sigma = 0{\cdot}07$. The reference length scale shown in figure 14(*a*) represents 1 cm or $1/(12{\cdot}7)$ of the radius of the basin. Although somewhat confused, the observed pattern is dominated by two gyres centred in the western half of the basin. The mean circulation in the northwest gyre is clockwise (or anticyclonic), while that in the much weaker southwest gyre is counterclockwise.

Moore (1970) clarified the controversy regarding the misinterpretation of mean Eulerian currents as mean transports that has existed in some recent ocean circulation problems. Using a Rossby number expansion approach, Moore analysed the governing nonlinear equations for inviscid oscillatory motion in a variable depth rotating ocean, and found that the second-order Lagrangian mean velocity satisfies the linearized vorticity and continuity equations for unforced steady geostrophic motion.

Since the sliced-cylinder geometry possesses no closed geostrophic contours, Moore's result implies that the mean Lagrangian motion associated with each

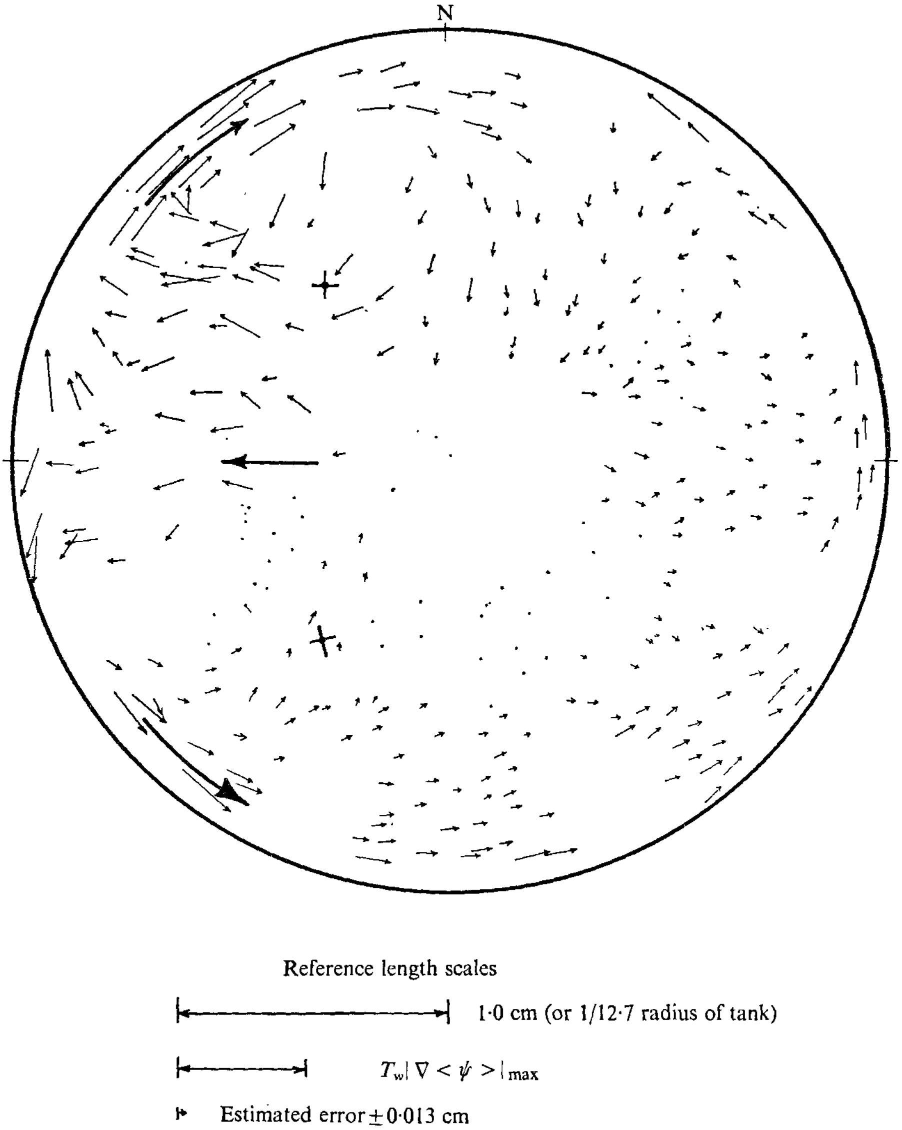

FIGURE 14(*a*). For legend see next page.

inviscid sliced-cylinder topographic Rossby mode is everywhere identically zero. Thus the mean Eulerian velocity field is exactly cancelled by the equal but opposite Stokes drift velocity field associated with the oscillatory wave motion. This result does *not* apply in general to forced motion in simple ocean systems with dissipation.

We present here a simple extension of Moore's (1970) analyses, to include the effects of periodic forcing and Ekman-layer dissipation. Consider f to be constant, the depth h variable, and a rigid lid enclosing the upper surface of the fluid. In keeping with the approximate vorticity balance governing the sliced-cylinder models, we assume that the periodic forcing and the Ekman dissipation coefficient

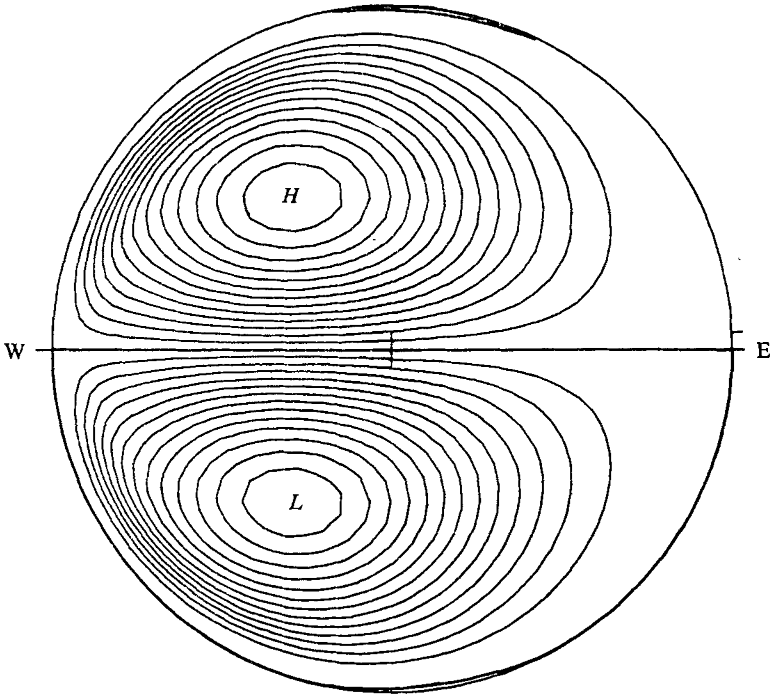

(b)

FIGURE 14. (a) Net mean Lagrangian particle displacement over one wave period, as measured by streak photography in the laboratory model, for $\epsilon_0 = 0{\cdot}0304$, $\omega/\Omega = 0{\cdot}07$, $Ek = 1{\cdot}38 \times 10^{-5}$. For meaning of large arrows, see text. P_w is the wave period. (b) Mean Eulerian stream function predicted numerically for same external conditions studied in (a). Contour interval is 10; extreme values are ± 138.

(equivalent to γ in (2)) are both spatially homogeneous. Then, in Moore's terminology, the governing scaled equations are

$$\frac{D}{Dt}\left(\frac{f+\epsilon\omega}{h}\right) = \frac{\epsilon b + \epsilon a\omega}{h^2}, \quad \nabla.(\mathbf{u}h) = 0,$$

where $a\omega$ and b represent the dissipation and forcing processes, and $\omega = \hat{\mathbf{k}}.\nabla \times \mathbf{u}$. Assume perturbation expansions for the velocity $\mathbf{u}$ and coefficients a and b of the form

$$(\mathbf{u}, a, b) = \sum_{n=1}^{\infty} \epsilon^n(\mathbf{u}_n, a_n, b_n).$$

Following Moore's procedure, we find from integration of the first-order vorticity equation that

$$\left[\frac{\omega_1}{h}\right]_{t_0}^{t} = -\int_{t_0}^{t}\left[\exp\left(\frac{a_1(t'-t)}{h}\right)\mathbf{u}_1.\nabla\left(\frac{f}{h}\right) - \frac{b_1}{h^2}\right]dt'.$$

Integration of the second-order vorticity equation, plus some manipulation, yields

$$\left\langle \mathbf{u}_2 + (\mathbf{u}_1^t.\nabla)\frac{\partial}{\partial t}\int_{t_0}^{t}\exp\left(\frac{a_1(t'-t)}{h}\right)\mathbf{u}_1(t')\,dt'\right\rangle.\nabla\left(\frac{f}{h}\right) = \frac{a_1\langle\omega_2\rangle}{h^2} - \left\langle \mathbf{u}_1^t.\nabla\frac{b_1}{h^2}\right\rangle, \quad (7)$$

where, in Moore's terminology, the superscript t indicates partial integration with respect to time from t_0 to t, and the brackets $\langle\ \rangle$ signify the time average over one wave period T from t_0 to $t_0 + T$.

The second-order *mean* Eulerian $\mathbf{U}_E$ and Lagrangian $\mathbf{U}_L$ velocities are defined by

$$\mathbf{U}_E = \langle \mathbf{u}_2 \rangle, \quad \mathbf{U}_L = \langle \mathbf{u}_2 \rangle + \langle (\mathbf{u}_1^t . \nabla) \mathbf{u}_1 \rangle. \tag{8), (9}$$

The second term in (9) is the Stokes drift velocity, discussed in depth by Longuet-Higgins (1969). Both $\mathbf{U}_E$ and $\mathbf{U}_L$ satisfy the continuity condition

$$\nabla . (h\mathbf{U}_E) = \nabla . (h\mathbf{U}_L) = 0.$$

Inspection of the mean vorticity equation (7) indicates that both mean Eulerian and Lagrangian flows exist for the case of strong forcing and dissipation (i.e. for both b_1 and a_1 of order unity). Only in the case of weak forcing and weak dissipation (i.e. b and a both $O(\epsilon)$, so that $a_1 = b_1 = 0$) does (7) reduce to Moore's result

$$\mathbf{U}_L . \nabla f/h = 0, \tag{10}$$

indicating a *zero* mean particle transport for basins with open geostrophic contours. As pointed out by Moore, this latter case applies to weakly driven systems with Ekman dissipation, provided the forcing frequency is near a strongly resonance eigenfrequency.

In the sliced-cylinder model equation (2), forcing and Ekman-layer dissipation are of equal order. The non-dimensional ratio of the damping to the local derivative of vorticity with respect to time is small. ($a\omega/\omega_t = \gamma/\sigma_{mn} = 0{\cdot}05$ for excitation at $\sigma = 0{\cdot}07$, near the maximum eigenfrequency σ_{01}.) But the appropriate Rossby number *Ro* is still smaller, suggesting that, at the larger resonance frequencies, the Stokes drift will partially cancel the second-order mean Eulerian velocity. If our experiments had been performed at much higher Ω, then a direct laboratory test of Moore's result could be attempted.

We shall attempt to test the suggestion that the mean particle transport will be reduced by the partial cancellation of the mean Eulerian flow by the Stokes drift when the lower resonant modes are excited. The numerical model was used to compute the mean Eulerian stream function for external parameters also used in the laboratory experiment of figure 14(a). The computed mean Eulerian field shown in figure 14(b) consists of two gyres, with a broad westward flow in the centre of the basin, fed by return flows from the northern and southern regions. The centres of the mean Eulerian gyres are located at the large crosses in figure 14(a). The maximum mean Eulerian currents occur in the western half of the basin along the negative x axis and in the northwest and southwest boundary regions. We have measured the local mean flow maximum as in these regions and plotted in figure 14(a), as the three large arrows, the calculated mean particle trajectory over one wave period assuming zero Stokes drift. The observed mean Lagrangian velocities are indeed smaller by approximately 60 %, indicating a substantial Stokes drift contribution to the Lagrangian transport.

3.4. *Steady and oscillatory forcing*

As mentioned above, several exploratory laboratory experiments were conducted to study the fluid response in the sliced-cylinder model to a forcing function possessing both steady and oscillatory components. A differential gear was used to add a sinusoidal and steady angular velocity together in the drive mechanism for the upper lid. The results of one experiment will be briefly discussed now. The experimental parameters are

$$\epsilon_s = 0{\cdot}06, \quad \epsilon_0 = 0{\cdot}03, \quad E = 1{\cdot}38\times 10^{-5}, \quad \sigma = 0{\cdot}07, \quad \tan\alpha = 0{\cdot}178.$$

The western boundary-layer Reynolds number $Re_w = \epsilon_s/(E^{\frac{1}{2}}\tan\alpha) = 91$ is significantly above the onset of instability value of 72 determined in Beardsley (1969). Two streak photographs with a phase lag of π between are shown in figure 15 (plate 2). The steady flow pattern with a western boundary layer is clearly dominated by the oscillatory mode. In the interior, the Sverdrup flow is approximately $\frac{1}{15}$ the oscillatory flow, while, in the western boundary current, the maximum steady velocity (theoretically predicted ignoring the oscillatory forcing) is 8 times the observed magnitude of the oscillatory mode (shown in figure 4, plate 1). For the case of cyclonic steady forcing ($\epsilon_s > 0$) shown here, the boundary layer alternately thickens and thins, depending on whether the topographic Rossby mode advects positive or negative vorticity into the western boundary current. The centre of the boundary-layer vortex (in the southwest quadrant) and the boundary transport clearly fluctuate, as does the directionality and magnitude of the flow in the western boundary-layer transition zone. The periodic production of secondary eddies for strong steady forcing are not observed here, owing to the domination by the driven oscillatory mode.

4. Conclusion

We have examined in parts 1 and 2 the response of the 'sliced-cylinder' wind-driven ocean circulation model when driven by a steady (part 1) or an oscillatory (part 2) 'wind' stress. In both cases, this simple model (devised by Pedlosky & Greenspan 1967) has exhibited many features both relevant to the wind-driven ocean circulation problem and of general interest in geophysical fluid dynamics. In the case of steady forcing, the competition between Ekman-layer suction and topographic vortex stretching for control of the Stewartson $E^{\frac{1}{4}}$ side-wall boundary layer has been elucidated; and the topographically modified $E^{\frac{1}{4}}$ layer has been used to close the interior 'wind' driven circulation on the western boundary of the basin. For strong steady forcing, the low-frequency flow instability observed in the sliced-cylinder model is now known to be due to the local breakdown of the finite-amplitude topographic Rossby wave embedded in the downstream transition region of the western boundary layer. In the case of a sinusoidal 'wind' stress, the expected resonance does occur when the spatial structural and frequency of the driving 'wind' stress is tuned to the more weakly damped (higher Q) topographic Rossby wave modes. The strong Stokes drift associated with the weakly-damped modes driven at and near resonance does partially oppose the mean

Eulerian motion, resulting in weaker Lagrangian transports. As indicated by Moore (1970), this point is quite important in deciding in particular cases if mean Lagrangian transports are driven by fluctuating motions. The generally good agreement between the laboratory observations and the numerical model predictions clearly verifies and illustrates the direct applicability of Greenspan's (1969) derivation of the two-dimensional governing vorticity equation for low-frequency flows in closed basins with small topographic variations. In reality, the wind stress field over the world ocean is quite complex: both significant mean and fluctuating components are still poorly understood. The preliminary observational evidence suggests that roughly half of the kinetic energy in the larger-scale oceanic eddies is contained in the baroclinic modes, rendering any barotropic model (like ours) incomplete at best. While the steep continental slopes should tend to effectively reflect incident planetary wave energy, the irregular boundary shape and topography together with baroclinic conversion processes (like baroclinic instability or the conversion of barotropic currents into topographically trapped baroclinic modes) make the time-dependent sliced-cylinder model discussed here much too simple for direct simulation of actual oceanic phenomena. But the very simplicity of the conceptual model has allowed us successfully to study and solve the barotropic problem in depth, with the realization that the results will help in the development and understanding of more sophisticated analytical and numerical models for the real wind-driven ocean circulation.

The author would like to acknowledge Dr M. Israeli of the MIT Mathematics Department, whose interest in the numerical aspects of this problem was very helpful and appreciated. I also want to acknowledge the continued help of Mrs B. Wysochansky and Mr S. Ricci in the preparation of this manuscript. The numerical experiments were conducted using the CDC 7600-6600 combined machine at the NSF supported National Center for Atmospheric Research. This research has been supported by the Office of Naval Research, grant N00014-67-A-0204-0048, and the National Science Foundation, grants GA-41073 and GA-41075.

REFERENCES

Beardsley, R. C. 1969 A laboratory model of the wind-driven ocean circulation. *J. Fluid Mech.* **38**, 255.

Beardsley, R. C. 1973 A numerical investigation of a laboratory analogy of the wind-driven ocean circulation. *Proc.* 1972 *NAS Symp. on Numerical Models of Ocean Circulation.*

Beardsley, R. C. & Robbins, K. 1975 The 'sliced cylinder' laboratory model of the wind-driven ocean circulation. Part 1. Steady forcing and topographic Rossby wave breakdown. *J. Fluid Mech.* **69**, 27–40.

Crease, J. 1962 Velocity measurements in the deep water of the western North Atlantic. *J. Geophys. Res.* **67**, 3173.

Greenspan, H. P. 1968 *The Theory of Rotating Fluids.* Cambridge University Press.

Greenspan, H. P. 1969 A note on the laboratory simulation of planetary flows. *Studies in Appl. Math.* **48**, 147.

Holton, J. 1971 An experimental study of forced barotropic Rossby waves. *J. Geophys. Fluid Dyn.* **2**, 323.

IBBETSON, A. & PHILLIPS, N. 1967 Some laboratory experiments on Rossby waves in a rotating annulus. *Tellus*, **19**, 81.

LAMB, H. 1945 *Hydrodynamics*. Cambridge University Press.

LONGUET-HIGGINS, M. S. 1969 On the transport of mass by time-varying ocean currents. *Deep-Sea Res.* **16**, 431.

MOORE, D. 1970 The mass transport velocity induced by free oscillations at a single frequency. *Geophys. Fluid Dyn.* **1**, 237.

MUNK, W. H. & MOORE, D. 1968 Is the Cromwell Current driven by equatorial Rossby waves? *J. Fluid Mech.* **33**, 241.

PEDLOSKY, J. 1965 A study of the time dependent ocean circulation. *J. Atmos. Sci.* **22**, 267.

PEDLOSKY, J. & GREENSPAN, H. P. 1967 A simple laboratory model for the oceanic circulation. *J. Fluid Mech.* **27**, 291.

PHILLIPS, N. 1965 Elementary Rossby waves. *Tellus*, **17**, 295.

PHILLIPS, N. 1966 Large-scale eddy motion in the western Atlantic. *J. Geophys. Res.* **71**, 3883.

ROBINSON, A. R. 1965 *Research Frontiers in Fluid Dynamics*, chap. 17, pp. 504–533. Interscience.

ROSSBY, C. *et al.* 1939 Relation between variations in the intensity of the zonal circulation of the atmosphere and the displacements of the semi-permanent centers of action. *J. Mar. Res.* **2**, 38.

SLATER, J. & FRANK, N. 1947 *Mechanics*. McGraw-Hill.

SWALLOW, M. 1961 Measuring deep currents in midocean. *New Scientist*, **9**, 740.

VERONIS, G. 1970 Effect of fluctuating winds on ocean circulation. *Deep-Sea Res.* **17**, 421.

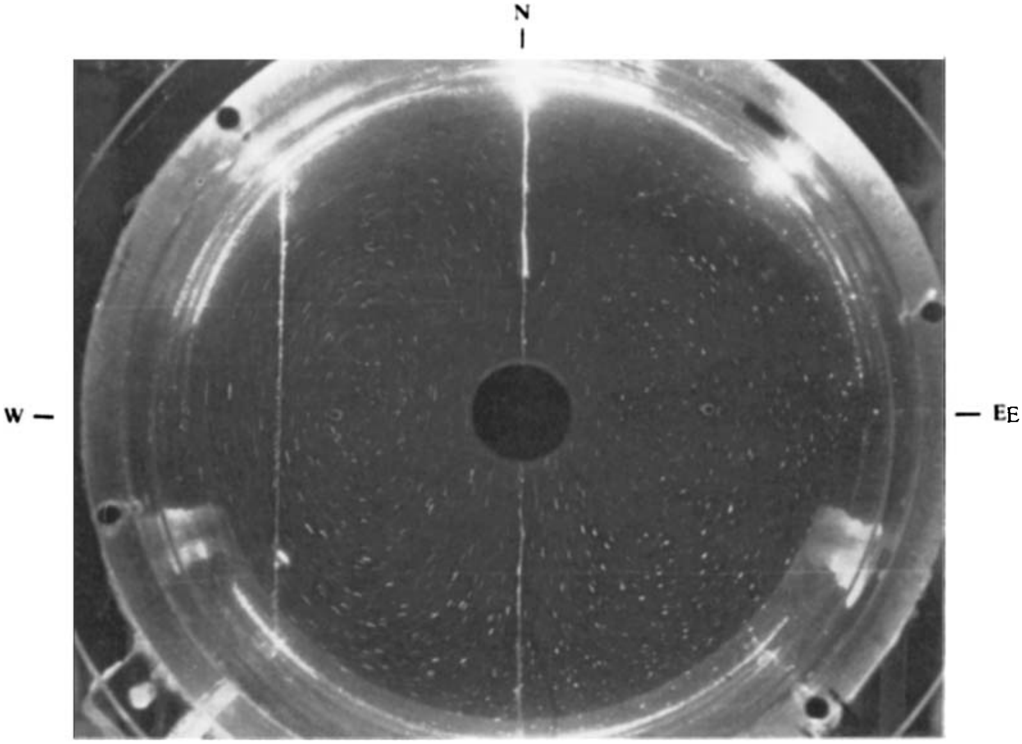

FIGURE 4. Streak photograph of horizontal velocity structure for $\epsilon_0 = 0{\cdot}0306$, $\omega/\Omega = 0{\cdot}07$.

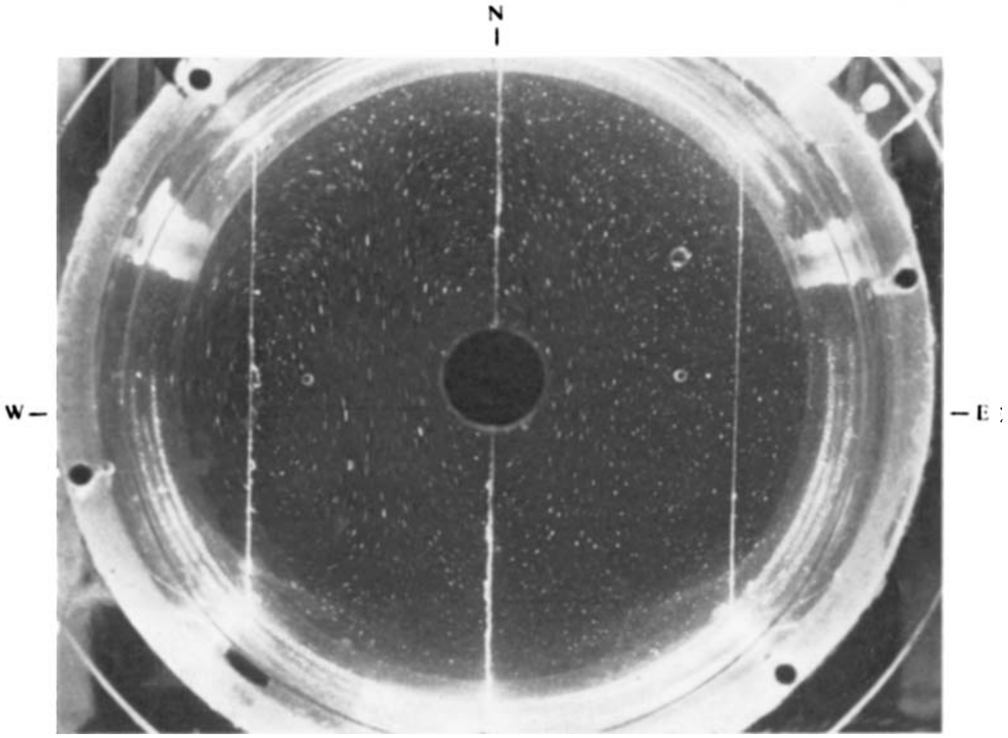

FIGURE 5. Streak photograph of horizontal velocity structure for $\epsilon_0 = 0{\cdot}024$, $\omega/\Omega = 0{\cdot}055$.

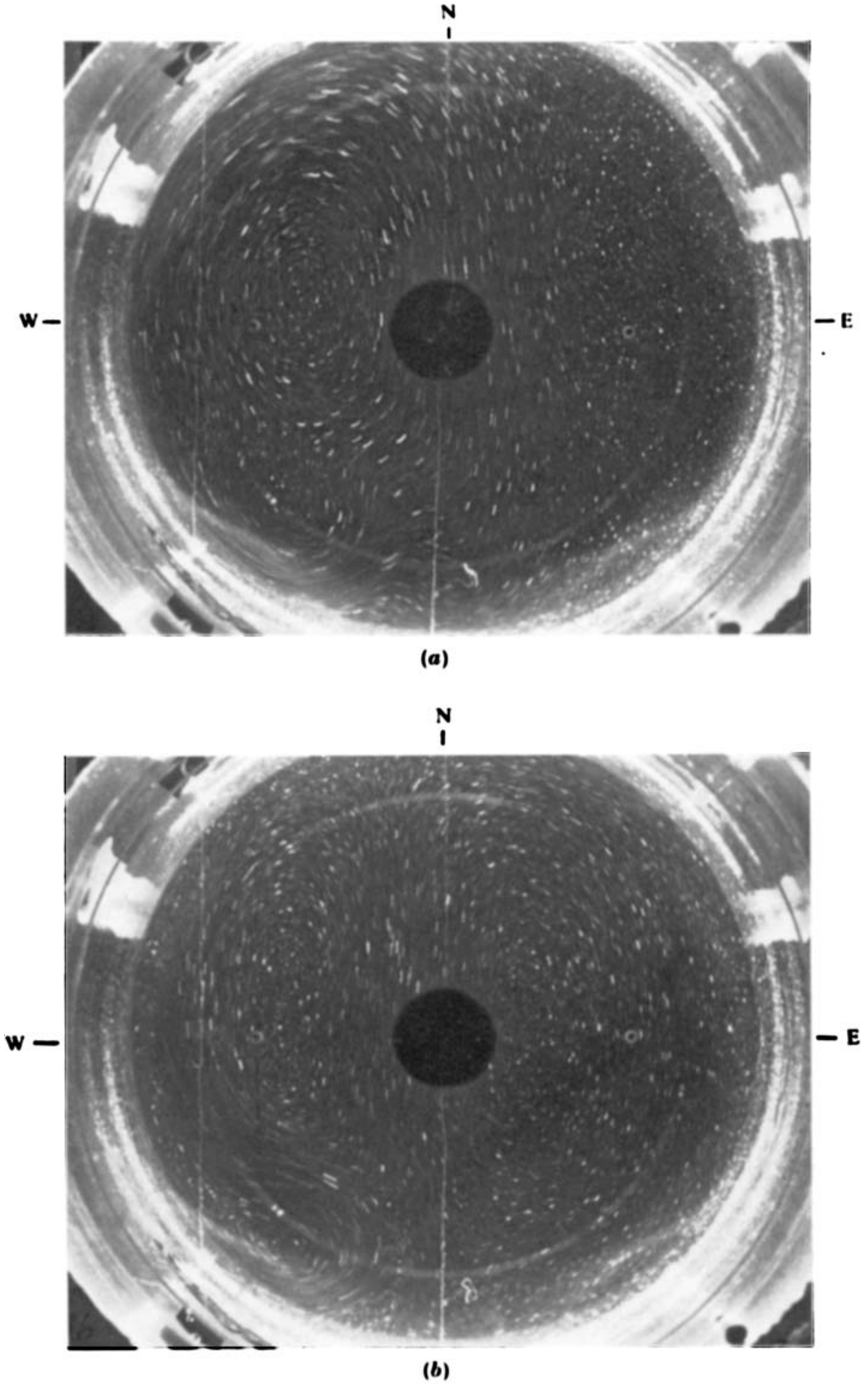

FIGURE 15. Streak photographs of horizontal velocity structure for combined steady and sinusoidal forcing, with $\epsilon_0 = 0{\cdot}03$, $\epsilon_5 = 0{\cdot}065$, $\omega/\Omega = 0{\cdot}07$. (*a*), (*b*) are separated in phase lag by approximately π.

BEARDSLEY